



## Structural Characterization of Heterogeneous Rh–Au Nanoparticles from a Microwave-Assisted Synthesis

Journal:	<i>Nanoscale</i>
Manuscript ID	NR-ART-06-2018-004866.R2
Article Type:	Paper
Date Submitted by the Author:	31-Oct-2018
Complete List of Authors:	Duan, Zhiyao; The University of Texas at Austin, Chemistry Timoshenko, Janis; Stony Brook University, Kunal, Pranaw; The University of Texas at Austin, Chemistry House, Stephen; University of Pittsburgh Wan, Haiqin; nanjing university, Jarvis, Karalee; The University of Texas at Austin, The Materials Science and Engineering Program Bonifacio, Cecile; University of Pittsburgh, Chemical and Petroleum Engineering Yang, Judith; University of Pittsburgh, Chemical and Petroleum Engineering Crooks, Richard; The University of Texas at Austin, Department of Chemistry Frenkel, Anatoly; Stony Brook University, Materials Science and Chemical Engineering Humphrey, Simon; The University of Texas at Austin, Chemistry & Biochemistry Henkelman, Graeme; The University of Texas at Austin, Chemistry

Cite this: DOI: 10.1039/xxxxxxxxxx

## Structural Characterization of Heterogeneous Rh–Au Nanoparticles from a Microwave-Assisted Synthesis<sup>†</sup>

Zhiyao Duan,<sup>a</sup> Janis Timoshenko,<sup>b</sup> Pranaw Kunal,<sup>c</sup> Stephen House,<sup>d</sup> Haqin Wan,<sup>c</sup> Karalee Jarvis,<sup>e</sup> Cecile Bonifacio,<sup>d</sup> Judith C. Yang,<sup>d,f</sup> Richard M. Crooks,<sup>e,g</sup> Anatoly I. Frenkel,<sup>h</sup> Simon M. Humphrey,<sup>e,i</sup> Graeme Henkelman,<sup>\*e,j</sup>

Received Date  
Accepted Date

DOI: 10.1039/xxxxxxxxxx

www.rsc.org/journalname

A microwave assisted method was used to synthesize RhAu nanoparticles (NPs). Characterization, based upon transmission electron microscopy (TEM), energy dispersive spectroscopy, and powder X-ray diffraction provided evidence of monomodal alloy NPs with a mean size distribution between 3 and 5 nm, depending upon composition. Extended X-ray adsorption fine-structure spectroscopy (EXAFS) also showed evidence of alloying, but the coordination numbers of Rh and Au indicated significant segregation between the metals. More problematic were the low coordination numbers for Rh; values of *ca.* 9 indicate NPs smaller than 2 nm – significantly smaller than those observed with TEM. Additionally, no single-particle structural models were able to reproduce the experimental EXAFS data. Resolution of this discrepancy was achieved with high resolution aberration corrected scanning TEM imaging which showed the presence of ultra-small (<2 nm) pure Rh clusters as well as larger (~3–5 nm) segregated particles with Au-rich cores and Rh-decorated shells. A heterogeneous model with a mix of ultrasmall pure Rh clusters and larger segregated Rh/Au NPs was able to explain the experimental measurements of the NPs over the range of compositions measured. The combination of density functional theory, EXAFS, and TEM allowed us to quantify the heterogeneity in the RhAu NPs. It was only through this combination of theoretical and experimental techniques that resulted in a bimodal distribution of particle sizes that was able to explain all of the experimental characterization data.

### 1 Introduction

Metal nanoparticles (MNPs) are important for catalysis both because they have a high surface area to volume ratio and because

<sup>a</sup> Department of Chemistry and the Institute for Computational Engineering and Sciences, The University of Texas at Austin, Austin, TX 78712-0165, USA.

<sup>b</sup> Department of Materials Science and Chemical Engineering, Stony Brook University, Stony Brook, NY, 11794-2275 USA.

<sup>c</sup> Department of Chemistry, The University of Texas at Austin, Austin, TX 78712-0165, USA.

<sup>d</sup> Department of Chemical and Petroleum Engineering, The University of Pittsburgh, Pittsburgh, PA 15261, USA.

<sup>e</sup> Texas Materials Institute, The University of Texas at Austin, Austin, TX 78712-0165, USA.

<sup>f</sup> Department of Physics and Astronomy, The University of Pittsburgh, Pittsburgh, PA 15261, USA.

<sup>g</sup> Department of Chemistry, The University of Texas at Austin, Austin, TX 78712-0165, USA. E-mail: crooks@cm.utexas.edu

<sup>h</sup> Department of Materials Science and Chemical Engineering, Stony Brook University, Stony Brook, NY, 11794-2275 USA. E-mail: anatoly.frenkel@stonybrook.edu

<sup>i</sup> Department of Chemistry, The University of Texas at Austin, Austin, TX 78712-0165, USA. E-mail: smh@cm.utexas.edu

<sup>j</sup> Department of Chemistry and the Institute for Computational Engineering and Sciences, The University of Texas at Austin, Austin, TX 78712-0165, USA. Fax: +1 512 471 8696; Tel: +1 512 471 4170; E-mail: henkelman@utexas.edu

<sup>†</sup> Electronic Supplementary Information (ESI) available: [details of any supplementary information available should be included in your journal article].

the catalytic properties of nanosized noble metals can be significantly different from bulk materials.<sup>1</sup> A tremendous amount of research in catalysis focuses on MNPs containing more than one component.<sup>2–4</sup> It has been shown, for example, that the use of two or more metals can tune the catalytic properties of MNPs and even result in properties that are significantly different from those of the individual components.<sup>5,6</sup> Correlations between the structure and function of alloy metal MNPs have been understood in terms of strain in the surface layer, electronic or ligand interactions between components, and the presence of under-coordinated sites and specific ensembles on the MNP surface. Notably, by exploiting properties unique to the nanoscale, unusual solid-solution alloy MNPs can be accessed between noble metals that are immiscible (or metastable) in the bulk, and therefore previously unstudied. Here, we consider one such case involving nanosized RhAu mixtures. Rh and Au are immiscible in the bulk over the entire composition range, preferring to undergo segregation from liquid co-melts below 2158 K. The RhAuNPs used in this study were made using a microwave assisted method reported recently,<sup>7</sup> and then a range of characterization and modeling techniques are used to try to understand the structure of the resulting RhAuNPs.

RhAu particles have been made previously both in our group<sup>7</sup> and by others using solution-phase approaches.<sup>8</sup> Piccolo *et al.* reported a significant segregation of the Rh and Au in the alloy particles.<sup>8</sup> In our previous studies, using the same microwave synthesis that is used here, we found that a random alloy model was in agreement with X-ray diffraction data and could be used to understand the enhanced activity of these species when supported on SiO<sub>2</sub>, in the vapor-phase hydrogenation of cyclohexene.<sup>7</sup> Here, we aim to gain a deeper understanding of the detailed structures of these particles as a step towards a better understanding of how they function as catalysts. As we will show, the synthesized RhAu particles are clearly heterogeneous in both size and composition, which poses formidable challenges for either ensemble-averaging characterization methods, including X-ray absorption fine structure (XAFS), as well as imaging methods, including TEM. Fortunately, these two types of methods can provide complementary structural information; thus, it is increasingly common to utilize a combination of methods to accurately describe the structural complexities that are inherent in these complex nanoscale systems.<sup>9</sup> In this study, we employ a similar philosophy to analyze the structure of the RhAu NPs in terms of size, composition, and elemental distribution. We also extend the structural characterization to fully atomic models by reproducing EXAFS spectra with atomistic simulations. Perhaps the most interesting aspect of this work is that initial attempts at characterization misled us, and only through the use of a range of characterization techniques combined with modeling are we finally able to present a structural model which is in complete agreement with all the data. To highlight this aspect of the work, the results are described as they were obtained.

**Table 1** Elemental composition values of Rh<sub>x</sub>Au<sub>1-x</sub>NPs as determined by different characterization techniques.

sample	EDS	XAS	ICP-OES
Rh <sub>0.3</sub> Au <sub>0.7</sub>	0.29:0.71	–	0.18:0.82
Rh <sub>0.5</sub> Au <sub>0.5</sub>	0.56:0.44	0.62:0.38	0.41:0.59
Rh <sub>0.7</sub> Au <sub>0.3</sub>	0.70:0.30	0.84:0.16	0.55:0.45
Rh <sub>0.9</sub> Au <sub>0.1</sub>	0.97:0.03	0.87:0.13	0.84:0.16

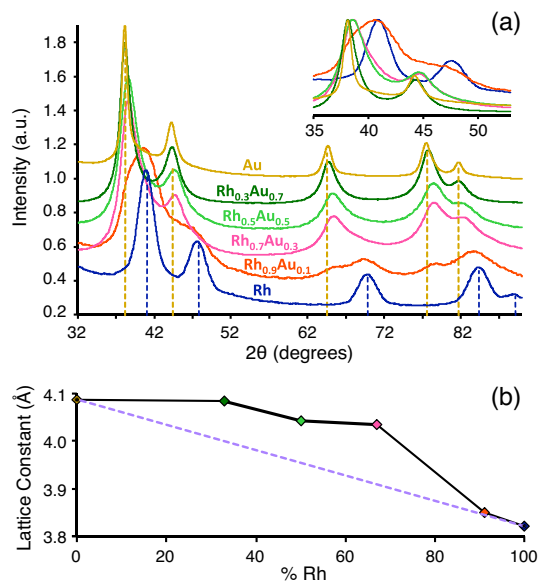


**Fig. 1** (a) PXRD data of Rh<sub>x</sub>Au<sub>1-x</sub> alloy NPs. Rh and Au reference peaks are shown as dashed lines in blue and gold respectively. (b) Variation of lattice constants with composition of RhAu alloy NPs; dashed purple line shows trend with theoretical values calculated using Vegard's law. Different colored points correspond to various compositions obtained using ICP-OES.

## 2 Results and Discussion

### 2.1 Synthesis

Rh<sub>x</sub>Au<sub>1-x</sub>NPs were synthesized using a microwave-assisted technique. All microwave assisted reactions were carried out inside a custom-designed microwave cavity as reported previously.<sup>7</sup> Briefly, Rh(III) and Au(III) metal salts were dissolved in ethylene glycol with a nominal molar ratio based on the desired NP composition. The metal salts were directly co-injected at a controlled rate into a stirred EG solution held at 150 °C, containing poly(vinylpyrrolidone) and NaBH<sub>4</sub>. After 30 minutes, the mixture was quenched in ice water and the resulting NPs were purified in acetone.

A set of RhAuNPs with nominal compositions were synthesized {0.3:0.7, 0.5:0.5, 0.7:0.3, 0.9:0.1}, as determined by the ratio of metal precursors. The Rh-rich samples were the focus of our characterization because that range of compositions was previously found to be most active for hydrogenation reactions.<sup>7</sup> The actual composition of the NPs were measured independently using ICP-OES, XAS, and STEM-EDS; the measured Rh:Au ratios are shown in Table 1. The ICP-OES and STEM-EDS analyses resulted in somewhat higher Au compositions as compared to the nominal (target) compositions, while the XAS showed higher Rh ratios.

Powder X-ray diffraction (PXRD, Figure 1a) was used to measure the lattice spacing of the NPs. The fact that intermediate compositions of  $\text{Rh}_x\text{Au}_{1-x}$  NPs show continuous peak shifts between those of the component metals was a factor that led us to believe that Rh and Au were randomly alloyed/well mixed in the NPs.<sup>7</sup> A plot of the lattice constant as a function of composition, derived using the Scherrer equation, is shown in Figure 1b. A homogeneous alloy would follow Vegard's law (dashed line). While our NPs are clearly not perfect alloys, the continuous lattice constant shift is evidence for alloying between Rh and Au.

## 2.2 TEM Characterization

Low-resolution TEM (Figure 2) shows that the average measured RhAuNP size increases with increasing Au content, ranging between 3–5 nm. The more Au-rich NPs are also more polydisperse. Note that for all NP compositions, the size distributions are monomodal, which we felt should justify the identification of a single NP with a characteristic size and composition.

Our PXRD analysis shows a varying degree of peak broadening for the RhAuNPs. Notably, significant peak broadening is seen for  $\text{Rh}_{0.9}\text{Au}_{0.1}$  NPs, which indicates the presence of small NPs. However, such NPs were not seen in our low-resolution TEM analysis (size distribution graph, Figure 2). High-resolution STEM was subsequently used, which gave a clear picture of small nanoclusters, as discussed below.

High-resolution TEM images of  $\text{Rh}_{0.5}\text{Au}_{0.5}$  NPs in Figure 3a reveal roughly spherical (cuboctahedral) particles ranging from 2 to 5 nm. The EDS maps in Figure 3b, c show co-localization of Au and Rh in these particles. A line scan through a single particle, imaged with high-angle annular dark-field scanning TEM (HAADF-STEM) (Figure 4) shows that the distribution of Rh and Au is not uniform, with Au favoring the core and Rh favoring the shell in the particle as imaged.

## 2.3 XANES analysis

Normalized X-ray adsorption near-edge structure (XANES spectra) for the Au  $L_3$ -edge and the Rh K-edge are shown in Figures 5a and b, respectively. XAS analysis was performed on the  $\text{Rh}_{0.9}\text{Au}_{0.1}$ ,  $\text{Rh}_{0.7}\text{Au}_{0.3}$ , and  $\text{Rh}_{0.5}\text{Au}_{0.5}$  samples. XANES spectra of all samples bear a strong resemblance to metallic Rh. Only the XANES spectra for the  $\text{Rh}_{0.5}\text{Au}_{0.5}$  NPs show that the as-prepared sample may be oxidized, as evidenced by the shift of the absorption edge and the features at low interatomic distances in the corresponding EXAFS spectrum, shown in Figure 5f. When the sample was mildly heated in an atmosphere of  $\text{H}_2$  gas, it was noted that the fraction of oxide decreased (as evidenced by the shift of the XANES edge closer to the rest of the samples). The EXAFS results obtained for the as-prepared and  $\text{H}_2$ -treated sample are very similar, however, suggesting that the influence of oxide fraction (if any) is minor. Therefore we discuss only the results obtained for the untreated sample.

The Au  $L_3$ -edge XANES data resemble Au foil. For the purposes of our structural characterization, it is particularly important to notice that even though the majority of atoms in the samples are Rh, the XANES spectra for the Au atoms are close to that of bulk

Au, suggesting some segregation of Au atoms.

## 2.4 EXAFS analysis

The structural parameters obtained from a fit of both the Rh and Au EXAFS data are summarized in Table 2. The experimental and fitted spectra (Figure S1) show excellent agreement. The EXAFS-fit structural parameters suggest that Rh and Au atoms are at least partially segregated. For all samples, both the Rh K-edge and Au  $L_3$ -edge EXAFS spectra are dominated by monometallic contributions. Even for the Rh-rich samples, the Au–Au coordination number exceeds that for Au–Rh by factors of 2–6. For a random alloy the ratio of the Au–Au coordination number to the Au–Rh coordination number should be equal to the molar ratio of Au to Rh atoms in the particles.<sup>10</sup> For example, in the  $\text{Rh}_{0.7}\text{Au}_{0.3}$  sample where Rh exceeds Au by more than a factor of two, the Au–Au coordination number should be half that of Au–Rh, and yet it was found to be double. These EXAFS data indicate that a homogeneous alloy is not a good model for the RhAu particles and that there must be Au-rich regions and Rh-rich regions, which enhanced the homometallic coordination numbers.

Nevertheless, the contribution of Au–Rh bonds was important to obtain a good fit to the experimental data, indicating that some fraction of Rh is indeed alloyed with Au. In addition, the Au–Au distance in all samples is about 0.03 – 0.04 Å smaller than that of bulk Au. For particles of this size (*ca.* 3 nm, according to TEM) there should not be such a large difference in the Au–Au bond length if the particles were pure Au.<sup>11</sup> The observed reduction in interatomic distances can be explained by Au–Rh alloying, because Rh has a smaller lattice constant than Au. Another possibility is that Au–Rh bonding could occur at the interface of segregated Au and Rh domains.

In addition, we found that the total Rh coordination number ( $N_{\text{Rh–Rh}} + N_{\text{Rh–Au}}$ ) is surprisingly small for the  $\text{Rh}_{0.7}\text{Au}_{0.3}$  and  $\text{Rh}_{0.5}\text{Au}_{0.5}$  NPs (6.8 and 5.6, respectively). For a model approximating the ensemble by a single representative particle, coordination numbers this low should correspond to particles smaller than 2nm.

## 2.5 STEM Characterization

The apparent discrepancy between TEM, PXRD, and EXAFS characterization prompted our employment of high-resolution aberration-corrected STEM (AC-STEM) analysis. The aim was to resolve the apparent disagreement between what appeared to be a monomodal distribution of alloy nanoparticles from TEM and PXRD with the largely segregated NPs with oddly low coordination numbers, as indicated by EXAFS that suggested a size inconsistent with the TEM images. Our analysis focused on the 0.5:0.5 and 0.9:0.1 Rh/Au samples.

Conventional S/TEM imaging was performed using a JEOL JEM 2100F at the Nanoscale Fabrication and Characterization Facility (NFCF) at the University of Pittsburgh and an FEI Talos F200X at the Center for Functional Nanomaterials (CFN) at Brookhaven National Laboratory. Initial measurements indicated sizes of  $2.48 \pm 0.91$  nm and  $3.18 \pm 0.53$  nm for the  $\text{Rh}_{0.5}\text{Au}_{0.5}$  and  $\text{Rh}_{0.9}\text{Au}_{0.1}$  samples, respectively. A wide spread of sizes, how-

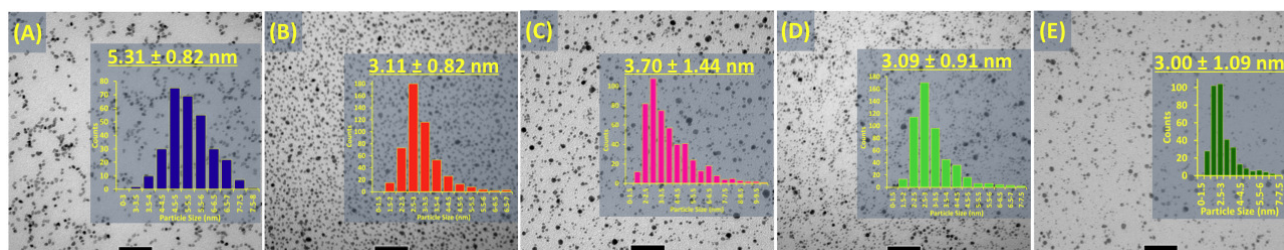


**Fig. 2** TEM images and size distributions of NPs: (a) Rh, (b) Rh<sub>0.9</sub>Au<sub>0.1</sub>, (c) Rh<sub>0.7</sub>Au<sub>0.3</sub>, (d) Rh<sub>0.5</sub>Au<sub>0.5</sub>, and (e) Rh<sub>0.3</sub>Au<sub>0.7</sub>. The black scale bars indicate 50 nm.

**Table 2** Values of structural parameters (Rh–Rh, Rh–Au, Au–Au and Au–Rh coordination numbers  $N$ , average interatomic distances  $\langle R \rangle$ , and Debye-Waller factors  $\sigma^2$ ) for the first coordination shell of Rh and Au atoms in the NPs obtained from the fits of Au L<sub>3</sub>-edge and Rh K-edge EXAFS data. Uncertainties in the last significant digits are given in parentheses.

	Rh foil	Au foil	Rh <sub>0.9</sub> Au <sub>0.1</sub> NPs	Rh <sub>0.7</sub> Au <sub>0.3</sub> NPs	Rh <sub>0.5</sub> Au <sub>0.5</sub> NPs
$N_{\text{Rh-Rh}}$	12	–	8.7(4)	6.0(3)	4.6(2)
$N_{\text{Rh-Au}}$	–	–	0.3(1)	0.8(5)	1.0(2)
$N_{\text{Au-Au}}$	–	12	7(1)	8(1)	8.8(3)
$N_{\text{Au-Rh}}$	–	–	2.2(7)	4(2)	1.5(2)
$\langle R \rangle_{\text{Rh-Rh}}$ (Å)	2.682(1)	–	2.680(1)	2.681(1)	2.686(2)
$\langle R \rangle_{\text{Rh-Au}}$ (Å)	–	–	2.74(1)	2.79(2)	2.786(5)
$\langle R \rangle_{\text{Au-Au}}$ (Å)	–	2.861(5)	2.821(5)	2.829(3)	2.833(1)
$\langle R \rangle_{\text{Au-Rh}}$ (Å)	–	–	2.74(1)	2.79(2)	2.786(5)
$\sigma_{\text{Rh-Rh}}^2$ ( $10^{-2}\text{Å}^2$ )	0.36(2)	–	0.58(2)	0.61(2)	0.67(5)
$\sigma_{\text{Rh-Au}}^2$ ( $10^{-2}\text{Å}^2$ )	–	–	1.0(2)	2(1)	0.9(1)
$\sigma_{\text{Au-Au}}^2$ ( $10^{-2}\text{Å}^2$ )	–	0.78(2)	1.0(1)	1.06(8)	0.87(3)
$\sigma_{\text{Au-Rh}}^2$ ( $10^{-2}\text{Å}^2$ )	–	–	1.0(2)	2(1)	0.9(1)

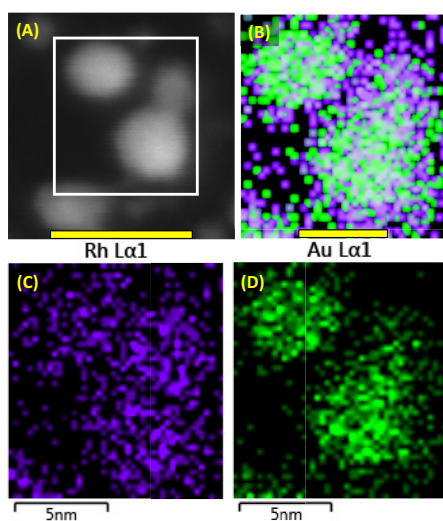


**Fig. 3** (a) HAADF-STEM micrograph of  $\text{Rh}_{0.5}\text{Au}_{0.5}$  NPs. The scale bar is 10 nm. (b) EDS elemental map showing the overlaid spatial distributions of Au (green) and Rh (purple) in the selected area indicated by the white rectangular box in (a); the scale bar is 5 nm. (c) and (d) show the individual EDS maps of Au and Rh, respectively.

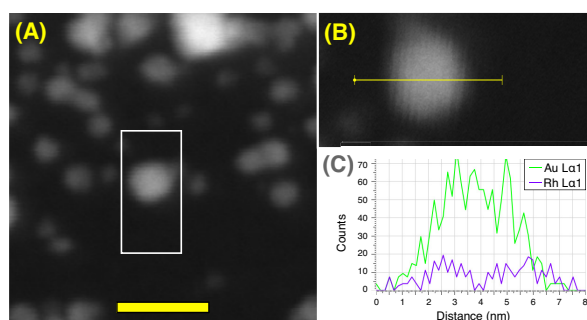


**Fig. 4** (a) High-angle annular dark-field STEM (HAADF-STEM) image of  $\text{Rh}_{0.5}\text{Au}_{0.5}$  NPs, scale bar is 10 nm; (b) 2D EDS mapping results of the selected area indicated by the white rectangular box in (a); (c) and (d) show an EDS line scan across a single NP.

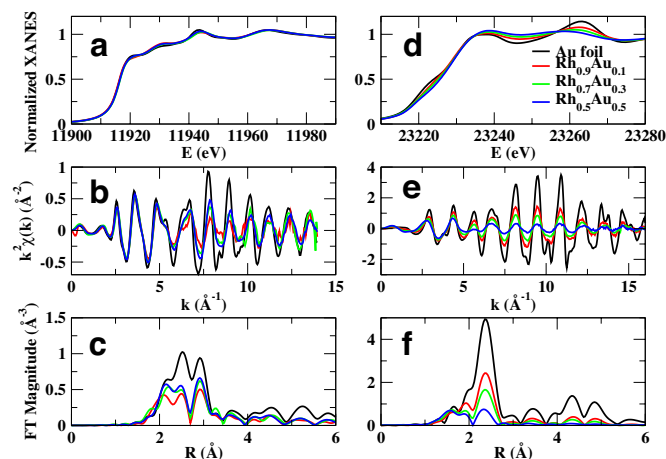


**Fig. 5** Au  $L_{3}$ -edge (left column) and Rh K-edge (right column) EXAFS spectra for the Au and Rh foils and for as-prepared Rh–Au NPs samples. Experimental XANES spectra (a,d) EXAFS spectra (b,e) and their Fourier transforms (FT) (c,f) are shown.

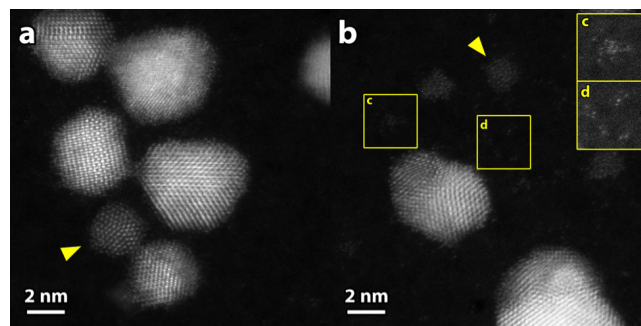


**Fig. 6** HAADF-STEM micrographs of the (a) 0.5:0.5 and (b) 0.9:0.1 Rh/Au systems. The arrowheads indicate examples of small ( $\leq 2$  nm), pure-Rh NPs. The insets (c and d) are regions of (b) that have been enlarged and increased in contrast to enhance the visibility of the (c) ultrasmall clusters and (d) non-associated atoms.

ever, from about 1–8 nm were observed. This analysis is consistent with what we found previously.

An FEI Themis 300 aberration-corrected S/TEM – usage courtesy of FEI – was subsequently employed to achieve the necessary spatial resolution both for imaging and energy-dispersive X-ray spectroscopy (EDS) mapping of the elemental composition. Equipped with a high-brightness gun and Super-X EDS, this microscope enabled single-atom resolution (Figure 6) and intra-particle composition mapping of nanometer-sized particles (Figure 7). This examination revealed highly heterogeneous, multi-modal morphologies: larger ( $\sim 3$ –10 nm), core-shell-like Rh/Au NPs (Au@Rh); smaller (1–3 nm) unalloyed Rh-only NPs; and a Rh-rich background of sub-nm clusters and non-associated individual atoms (e.g., Figure 6b insets). Both the NP size and relative abundance of particle type depended on the stoichiometry, and for the larger, mixed-metal particles, their morphology and composition varied with stoichiometry, as well. In the 0.5:0.5 system, the larger, mixed-metal particles consisted of Au-rich cores with Rh-rich shells, with overall compositions near the nominal stoichiometry. These shells were not always continuous, sometimes exhibiting a preferential attachment of the Rh to certain facets of the Au cores (e.g., Figure 7, white arrow). The integrated EDS signal from the non-NP portions of the maps was found to be Rh-rich (69–83 at.% Rh), confirming that the ultrasmall clusters and non-associated atoms were predominately Rh. In the 0.9:0.1 system, the mixed-metal particles appeared more strongly phase segregated, approaching a more Janus particle-like arrangement. These particles were also significantly Au-enriched (37–71 at.% Au). Correspondingly, the relative number of smaller Rh-only NPs was greater, and the background signal (ultrasmall clusters and non-associated atoms) was even richer in Rh (76–86 at.%). These TEM results provided the necessary information to develop heterogeneous multi-particle models that agree significantly better with the EXAFS spectra (see below).

## 2.6 Quantitative structure model for Rh–Au NPs

Based on the heterogeneity in NP size and composition observed with AC-S/TEM, we propose a model in which there are two different types of NPs present in the sample: (a) ultrasmall ( $< 2$  nm)

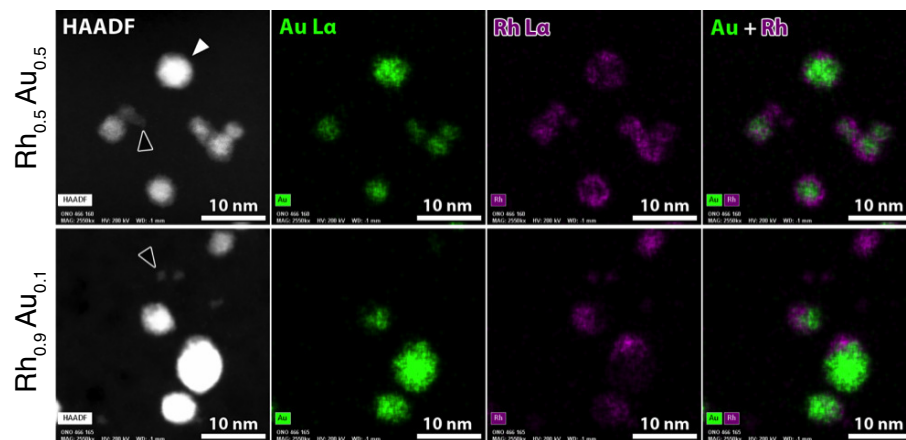


**Fig. 7** Energy-dispersive X-ray spectroscopy (EDS) elemental maps of the (upper) 0.5:0.5 and (lower) 0.9:0.1 Rh/Au systems. The black arrowheads indicate examples of small, pure-Rh NPs. The white arrowhead indicates a particle with preferential attachment of Rh to certain facets of the Au-rich core.

particles of pure Rh; (b) larger ( $\sim 5$  nm) NPs that contain both Rh and Au. Further we attempt to understand from available EXAFS and microscopy data the structure of these larger particles in more detail.

The parameters of our model include the size of the large and small particles, their ratio in the sample, the elemental composition of the large particles, and the degree to which Au and Rh are segregated from each other and to the surface of the large NP. For a comparison with the measured EXAFS data, the size of the particles is expressed in terms of the total coordination number of metal atoms in the large particles,  $N_{M-M,L}$  and the small particles,  $N_{M-M,S}$ . In this notation,  $M$  indicates the total contribution from Au and Rh and L or S indicates the large or small particle. The fraction of metal atoms in the large particles is defined as  $X_L$ . Then, it is possible to calculate the average coordination numbers that would be measured from a population of both particles,

$$N_{\text{Au-Au}} = \frac{S_{\text{Au-Rh}} X_{\text{Au,L}} S_{\text{Au-surf}}}{X_{\text{Au,L}} S_{\text{Au-surf}} + 1 - X_{\text{Au,L}}} N_{\text{M-M,L}} \quad (1)$$

$$N_{\text{Au-Rh}} = \frac{(1 - S_{\text{Au-Rh}} X_{\text{Au,L}}) S_{\text{Au-surf}}}{X_{\text{Au,L}} S_{\text{Au-surf}} + 1 - X_{\text{Au,L}}} N_{\text{M-M,L}} \quad (2)$$

$$N_{\text{Rh-Au}} = \frac{X_{\text{L}} X_{\text{Au,L}} (1 - S_{\text{Au-Rh}} X_{\text{Au,L}}) S_{\text{Au-surf}}}{(1 - X_{\text{L}} X_{\text{Au,L}}) (X_{\text{Au,L}} S_{\text{Au-surf}} + 1 - X_{\text{Au,L}})} N_{\text{M-M,L}} \quad (3)$$

$$N_{\text{Rh-Rh}} = \frac{X_{\text{L}} N_{\text{M-M,L}} (1 - X_{\text{Au,L}} - S_{\text{Au-surf}} X_{\text{Au,L}} + S_{\text{Au-Rh}} S_{\text{Au-surf}} X_{\text{Au,L}}^2)}{(X_{\text{Au,L}} S_{\text{Au-surf}} + 1 - X_{\text{Au,L}}) (1 - X_{\text{L}} X_{\text{Au,L}})} + \frac{(1 - X_{\text{L}}) N_{\text{M-M,S}}}{1 - X_{\text{L}} X_{\text{Au,L}}}, \quad (4)$$

where  $X_{\text{Au,L}}$  is the elemental fraction of Au in the large particles, and

$$S_{\text{Au-Rh}} = \frac{N_{\text{Au-Au,L}}}{N_{\text{Au-M,L}}} \frac{1}{X_{\text{Au,L}}} \quad (5)$$

is a compositional segregation parameter, defined as the relative probability of Au–Au neighbors as compared a random alloy where  $S_{\text{Au-Rh}} = 1$ . The second segregation parameter,

$$S_{\text{Au-surf}} = \frac{N_{\text{Au-M,L}}}{N_{\text{Rh-M,L}}}, \quad (6)$$

is the relative probability of Au–M bonds as compared Rh–M bonds in the large NPs.  $S_{\text{Au-surf}} > 1$  indicates that Rh is favored on the surface of the large NPs and  $S_{\text{Au-surf}} < 1$  indicates that Rh is favored the NP core. We can now solve these equations for the NP structural parameters ( $X_{\text{L}}$ ,  $X_{\text{Au,L}}$ ,  $N_{\text{M-M,L}}$ ,  $N_{\text{M-M,S}}$ ) as a function of the two segregation parameters,  $S_{\text{Au-Rh}}$  and  $S_{\text{Au-surf}}$ , using coordination numbers from EXAFS ( $N_{\text{Au-Au}}$ ,  $N_{\text{Au-Rh}}$ ,  $N_{\text{Rh-Rh}}$ , and  $N_{\text{Rh-Au}}$ ) and information on the particle sizes from S/TEM as input.

The values of  $N_{\text{M-M,L}}$  and  $N_{\text{M-M,S}}$  as functions of the segregation parameters  $S_{\text{Au-Rh}}$  and  $S_{\text{Au-surf}}$  are shown in Figure 8. For  $\text{Rh}_{0.9}\text{Au}_{0.1}$ , certain values of  $S_{\text{Au-Rh}}$  and  $S_{\text{Au-surf}}$  allow for the presence of Rh–Au NPs with size *ca.* 3 nm as well as the presence of ultrasmall Rh NPs with sizes below 1 nm, which are observed in the size-distribution from STEM. The corresponding region in the ( $S_{\text{Au-Rh}}$ ,  $S_{\text{Au-surf}}$ ) parameter space is highlighted by the green lines in Figure 8. These regions overlap for  $S_{\text{Au-Rh}}$  values between 3.5 and 5.5 and  $S_{\text{Au-surf}}$  values between 0.84 and 0.88. Hence, in this region, both EXAFS data and TEM data are in agreement for the  $\text{Rh}_{0.9}\text{Au}_{0.1}$  sample. The corresponding values for the structural parameters  $N_{\text{M-M,L}}$ ,  $N_{\text{M-M,S}}$ ,  $X_{\text{L}}$ , and  $X_{\text{Au,L}}$  are listed in Table 3. They indicate that about 60–80% of all atoms in the  $\text{Rh}_{0.9}\text{Au}_{0.1}$  sample are located within larger NPs (*ca.* 3 nm), while the remaining atoms reside in the pure Rh NPs with sizes below 1 nm. In the larger NPs, the Au concentration is only 10–20%. However, these Au atoms are concentrated in a few Au-rich regions indicated by  $S_{\text{Au-Rh}}$  values greater than 1. Smaller total coordination numbers for Au atoms than for Rh atoms in these larger NPs suggest that these Au-rich regions are located preferentially at the surface of larger NPs, although we note that there is a large uncertainty in the Au coordination numbers in this sample ( $N_{\text{Au-M}} = 9 \pm 2$ ), and that Au surface segregation is not observed with TEM.

A similar analysis for  $\text{Rh}_{0.5}\text{Au}_{0.5}$  and  $\text{Rh}_{0.7}\text{Au}_{0.3}$  are also shown

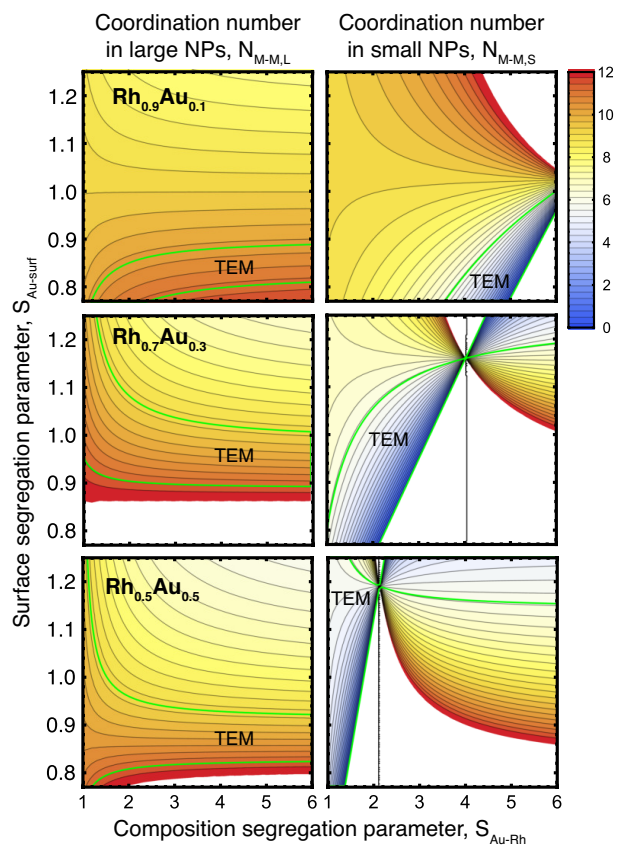


**Fig. 8** Calculated coordination numbers,  $N_{\text{M-M,L}}$  and  $N_{\text{M-M,S}}$  as functions of the compositional  $S_{\text{Au-Rh}}$  and surface  $S_{\text{Au-surf}}$  segregation parameters. The regions between the green lines correspond to the size distributions of large (left) and small (right) particles observed from STEM.



**Table 3** Average coordination numbers in the large Rh–Au NPs and ultrasmall Rh NPs ( $N_{M-M,L}$  and  $N_{Rh-Rh,S}$ ), relative concentration of Au atoms in the large NPs ( $X_{Au,L}$ ), the fraction of atoms within the large NPs ( $X_L$ ), compositional segregation parameter ( $S_{Au-Rh}$ ), and surface segregation parameter ( $S_{Au-surf}$ ).

	random alloy			segregated		
	Rh <sub>0.9</sub> Au <sub>0.1</sub>	Rh <sub>0.7</sub> Au <sub>0.3</sub>	Rh <sub>0.5</sub> Au <sub>0.5</sub>	Rh <sub>0.9</sub> Au <sub>0.1</sub>	Rh <sub>0.7</sub> Au <sub>0.3</sub>	Rh <sub>0.5</sub> Au <sub>0.5</sub>
$N_{M-M,L}$	9(1)	12(2)	10.3(4)	10.7(10)	10.2(7)	10(2)
$N_{M-M,S}$	9.0(4)	6.0(4)	5.0(2)	0–7	0–6	0–5
$X_{Au,L}$	0.76(6)	0.7(1)	0.85(2)	0.1–0.2	0.2–0.5	> 0.5
$X_L$	0.16(6)	0.3(1)	0.47(7)	0.6–0.9	0.3–0.8	< 0.8
$S_{Au-Rh}$	1	1	1	3.8–5.6	1.3–3.0	1.0–1.7
$S_{Au-surf}$	1	1	1	0.8–0.9	1.1–1.3	0.8–1.3

in Figure 8. Note that for Rh<sub>0.7</sub>Au<sub>0.3</sub> we do not have reliable information on the particle size distribution from STEM. Therefore, we assumed a similar broad particle size distribution as obtained for Rh<sub>0.5</sub>Au<sub>0.5</sub>. In contrast to Rh<sub>0.9</sub>Au<sub>0.1</sub>, one can see that the value of the compositional segregation parameter  $S_{Au-Rh}$  should be between 1 and 1.8 for Rh<sub>0.5</sub>Au<sub>0.5</sub> to ensure physically reasonable particle sizes and atom concentrations. This indicates some segregation of Au and Rh in Rh<sub>0.5</sub>Au<sub>0.5</sub> but less than in the Rh<sub>0.9</sub>Au<sub>0.1</sub> sample.

For Rh<sub>0.7</sub>Au<sub>0.3</sub> (without using STEM information) the acceptable values for the segregation coefficient  $S_{Au-Rh}$  can vary broadly, from  $S_{Au-Rh} = 1$  (no segregation in larger particles) to higher values with increased segregation. Interestingly, the surface segregation coefficient  $S_{Au-surf}$  is always larger than 1, indicating that Au does not favor the surface of NPs. This conclusion can also be seen from the total Au coordination number  $N_{Au-M,L}$ , which is equal to the bulk value of 12, indicating that Au is located predominantly below the NPs surface. Furthermore, if we assume that the particle size distribution is similar to that in the Rh<sub>0.5</sub>Au<sub>0.5</sub> sample, we can improve the range of acceptable parameter values. Both green regions in Figure 8 overlap in the  $S_{Au-Rh}$ -range between *ca.* 1.3 and 3.3, which suggests that Rh and Au segregation within the large particles in the Rh<sub>0.7</sub>Au<sub>0.3</sub> sample is more pronounced than in the Rh<sub>0.5</sub>Au<sub>0.5</sub> sample (with  $S_{Au-Rh}$  values below 1.8), but smaller than in the Rh<sub>0.9</sub>Au<sub>0.1</sub> sample (with  $S_{Au-Rh}$  values between 3.8 and 5.6).  $S_{Au-surf}$  values between 1.1 and 1.5 indicate that some Au had segregated toward the NP cores in the Rh<sub>0.7</sub>Au<sub>0.3</sub> sample. The total Au concentration in the large RhAu particles  $X_{Au,L}$  is then between 0.2 and 0.5 (somewhat larger than in the Rh<sub>0.9</sub>Au<sub>0.1</sub> sample, where the Au concentration is 0.1–0.2, but smaller than in Rh<sub>0.5</sub>Au<sub>0.5</sub> sample, where the Au concentration is above 0.5). Finally, the fraction of atoms in large NPs can vary in a broad range between 40 and 80%. Similar values were obtained for the other samples: for Rh<sub>0.5</sub>Au<sub>0.5</sub> less than 80% of the atoms are within the large particles, while for Rh<sub>0.9</sub>Au<sub>0.1</sub> there are between 60 and 80% of the atoms in the large particles.

## 2.7 Structure determination through atomistic simulation

TEM studies provide 2D projections of the morphologies and elemental distributions of Rh–Au NPs, while EXAFS analysis can give

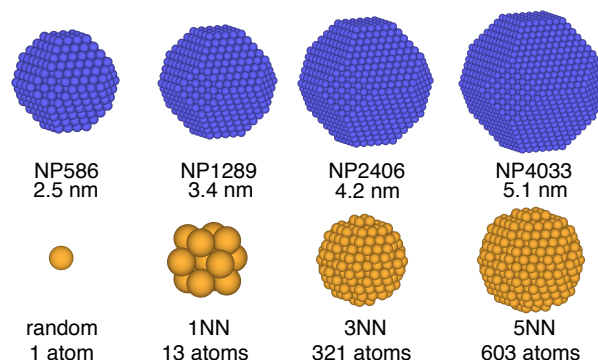


**Fig. 9** Atomic models used for structural screening. NPs were constructed using a Rh host in the size range from 2.5 to 5.1 nm. To these particles, Au regions were added (replacing Rh atoms) with grain sizes ranging from a single Au atom to the largest grains considered with 5 Au nearest neighbor shells (5 NN) containing a total of 603 atoms.

average values for local bonding information. However, both lack the ability to reconstruct NP structures with full atomic resolution. To achieve this goal, we performed atomistic simulations of the EXAFS spectra of various proposed structures of Rh–Au NPs. The structure with minimal difference to the experimental Rh K-edge and Au L<sub>3</sub>-edge EXAFS spectra is considered as the representative atomic structure for the synthesized RhAuNPs. The method has been successfully applied previously to characterize the atomic structure of Au DENS<sup>12,13</sup> and Co oxides.<sup>14</sup> Briefly, to obtain the EXAFS spectra of atomistic models, we developed an empirical potential for the RhAu binary system of the modified embedded-atom method (MEAM) form. Monte Carlo (MC) simulations were performed to generate an ensemble of equilibrium structures from which FEFF6-lite<sup>15</sup> was used to calculate the corresponding EXAFS spectra.

The candidate models used for the structural screening were constructed as follows. First, a host RhNP with truncated-octahedral shape was selected. The diameter of the Rh NPs range from 2.5 nm (586 atoms) to 5.1 nm (4033 atoms) assuming an FCC lattice constant of 3.8 Å. Au grains were then added to the selected Rh NP host. The size of the Au grains range from one single Au atom, corresponding to a random alloy, to a Au grain having a radius of five nearest-neighbor distances (5 NN), containing 603 atoms. The Au grains of different sizes were ran-

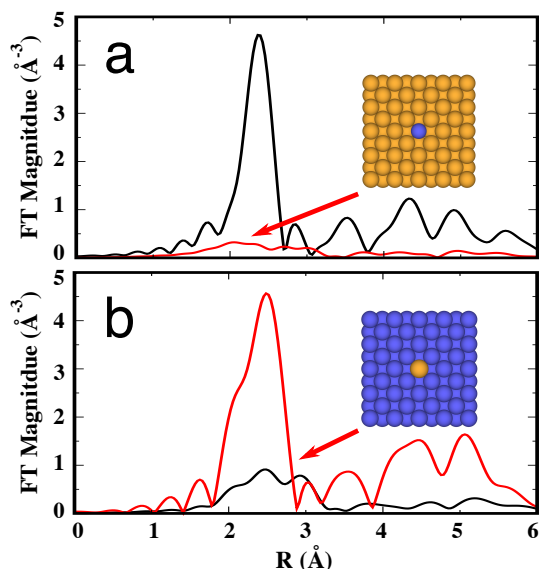


**Fig. 10** Alloying effect on EXAFS spectra of (a) Rh K- and (b) Au L<sub>3</sub>-edges. The black curves are for EXAFS spectra of (a) Rh bulk and (b) Au bulk. The red curves are for EXAFS spectra of (a) a single Rh atom in bulk Au and (b) a single Au atom in bulk Rh.

domly added to the Rh NP by replacing Rh atoms with Au to make a series of Rh/Au NPs with Au compositions ranging from 10 to 90%. In this way, atomic models of different compositions and degrees of phase segregation were constructed. Visualizations of Rh NPs and Au grains are shown in Figure 9. There were 144 proposed Rh/Au structures in total. The difference between the simulated and experimental EXAFS spectra was evaluated as  $\int_{r_{\min}}^{r_{\max}} |\text{FT}_{\text{mag}} k^2 \chi_{\text{sim}} - \text{FT}_{\text{mag}} k^2 \chi_{\text{exp}}| dr$ , where  $\text{FT}_{\text{mag}}$  is the magnitude of the complex Fourier transformation of the EXAFS spectra. This integral was evaluated for both the Rh K-edge and Au L<sub>3</sub>-edge, and a sum of both edges was used to calculate the difference between the experiment and the simulated model.

Before discussing the results, it is helpful to first get a sense for how alloying influences the EXAFS spectra of the Au L<sub>3</sub> and the Rh K-edge. To do this, we built FCC crystals for Rh and Au with their corresponding lattice constants. One atom in the Rh (Au) crystal was then changed to Au (Rh). The crystals with the impurities were equilibrated at 298 K and the EXAFS spectra of the impurities were evaluated. In Figure 10(a), it can be seen that the EXAFS spectrum of the Au impurity in a Rh crystal has significantly higher magnitude than the spectrum of a Au foil. The enhanced signal from the Au impurity can be attributed to the decreased dynamical Debye-Waller factor in the stiff Rh matrix as compared to bulk Au. Quantitatively, the Debye-Waller factor decreases from 0.84 to  $0.29 \times 10^{-2} \text{ \AA}^2$ . Similarly, the EXAFS spectrum of the Rh impurity in a Au crystal has a low magnitude comparing to Rh foil due to an increased Debye-Waller factor from 0.38 to  $0.90 \times 10^{-2} \text{ \AA}^2$ . These and other fit parameters are given in Table S3).

Our initial structural screening employed single NP models of nominal compositions to find candidate atomic structures consistent with the Rh<sub>0.9</sub>Au<sub>0.1</sub>, Rh<sub>0.7</sub>Au<sub>0.3</sub>, and Rh<sub>0.5</sub>Au<sub>0.5</sub> samples. The underlying assumption of the single NP model is that the synthe-

sized RhAu NPs are structurally homogeneous and can be accurately represented by a single NP. Since the composition of the proposed RhAu NPs were fixed to the nominal compositions, the variables are the size and degree of compositional segregation of the NPs. In order to identify the most significant differences between the single-particle model and the experimental EXAFS, we fit the simulated EXAFS from the single-particle model and looked to see which parameters varied most significantly as compared to experiment. The fitted EXAFS spectra along with the simulated spectra are shown in Figure S6 and the extracted structural parameters are summarized in Table S5.

The screening results are shown in Figure 11. For the Rh<sub>0.9</sub>Au<sub>0.1</sub> sample, the best model is a pure Rh NP of size 2.5 nm with 10% of Au in a segregated grain about 3 NN (321 atoms) in size. The Rh K-edge for this model matched the high magnitude of the Rh K-edge in the experimental EXAFS spectrum, indicating a Rh NP with little Au alloying. However, the predicted Rh-K edge was shifted to lower  $R$  as compared to the experiment. This could be an indication of more Au atoms in the NP as a greater number of Rh–Au bonds would increase the average Rh–M bond length longer. For the Au L<sub>3</sub>-edge, the match between experiment and simulation is not as good as the Rh K-edge. The magnitude of the Au L<sub>3</sub>-edge between 2–3 Å is higher than in the experiment. This discrepancy could be due to the overestimation of the portion of Au–Rh bonds out of the total Au–M bonds since Au–Rh bonding would cause the magnitude of the Au L<sub>3</sub>-edge to be higher as shown in Figure 10. The fitted structural parameters (shown in Table S5) also suggest that  $N_{\text{Rh–Rh}}$  and  $N_{\text{Au–Rh}}$  need to be decreased, while  $N_{\text{Au–Au}}$  needs to be increased to better match the experimental data. Considering the discrepancies for both the Rh K-edge and Au L<sub>3</sub>-edge in the Rh<sub>0.9</sub>Au<sub>0.1</sub> sample, the RhAu NPs should have more Au atoms present in larger Au grains. These discrepancies can be resolved by including the small pure Rh NPs observed by STEM, so that the larger NPs can be enriched with Au.

For the Rh<sub>0.7</sub>Au<sub>0.3</sub> sample, the predicted structure is a 4.2 nm NP with 5 NN Au grains. A similar discrepancy in the Au L<sub>3</sub>-edge is also present in the Rh<sub>0.9</sub>Au<sub>0.1</sub> sample. In contrast, for the Rh<sub>0.5</sub>Au<sub>0.5</sub> sample the predicted structure seems to underestimate the percentage of Au–Rh bonds since the simulated Au L<sub>3</sub>-edge has lower magnitude than the experiment. For this reason, the real Rh–Au NP should have more alloying. The single particle model for the Rh<sub>0.5</sub>Au<sub>0.5</sub> sample also overestimates the magnitude of Rh K-edge, which could also be improved by the inclusion of small pure Rh clusters. Sizable discrepancies can be observed (Table S5), especially for the Rh–Rh and Rh–Au coordination numbers. This is consistent with the fact that the best single-particle model is not able to capture the low Rh coordination numbers that are observed in the EXAFS data.

Including the heterogeneity of the ultrasmall Rh clusters yields a structural model that better reproduces the experimental EXAFS data. Specifically, we choose a two-particle model with (i) a fraction of small Rh<sub>38</sub> clusters and (ii) larger Rh–Au NPs constructed in the same way as for the single-NP model. The overall composition is constrained to the nominal composition during fitting. The Rh<sub>38</sub> structure is disordered as predicted by our MEAM potential

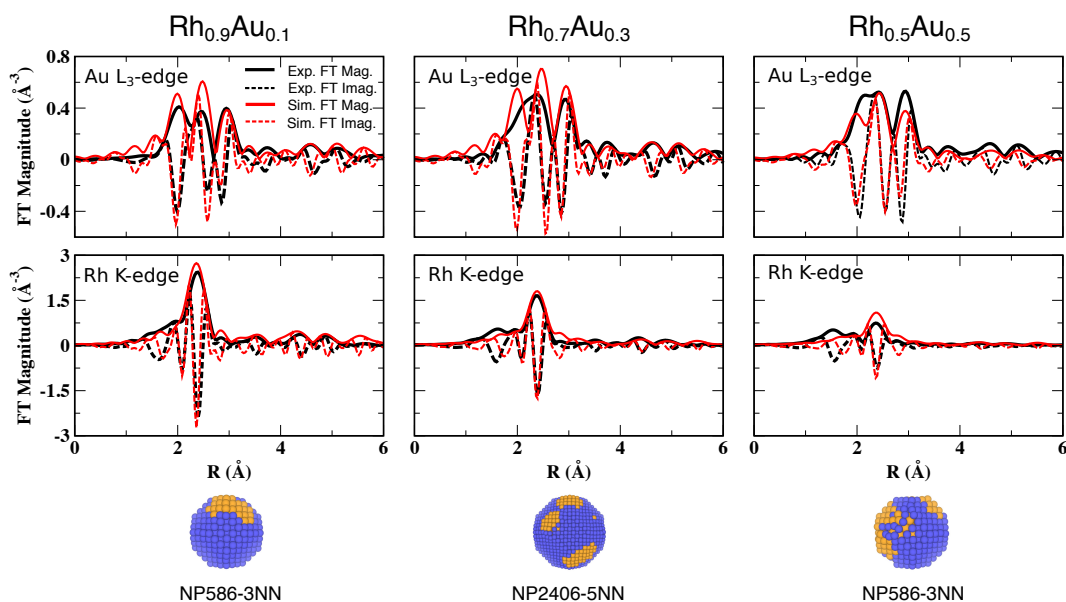


**Fig. 11** Comparison of experimental and simulated Au L<sub>3</sub>-edge and Rh K-edge EXAFS spectra. The best-fit single-NP models employed to simulate EXAFS spectra are shown for each case. Blue spheres represent Rh atoms; Gold are Au.

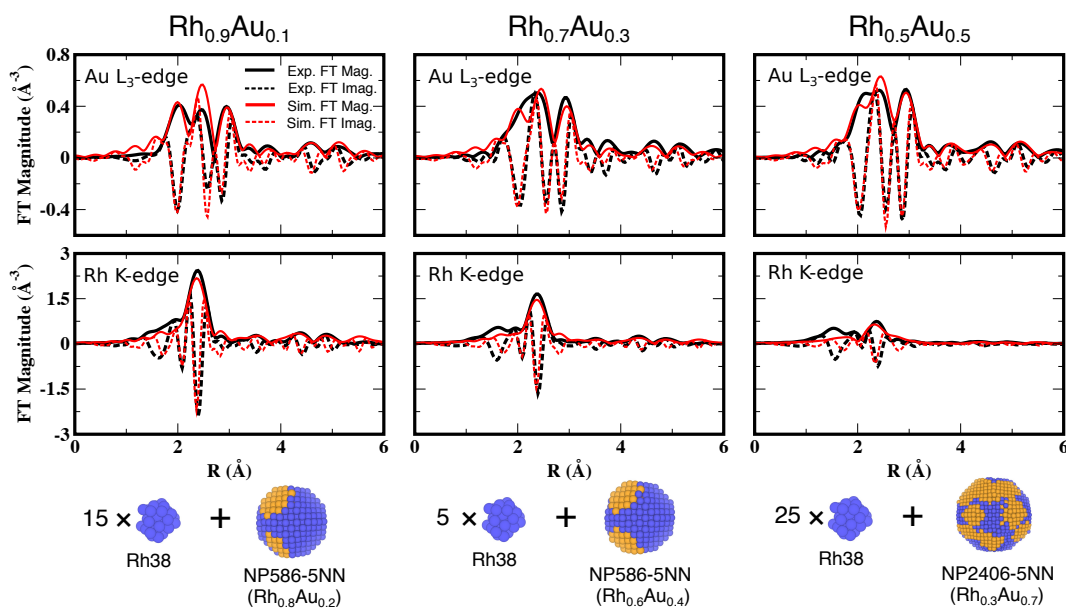


**Fig. 12** Comparison of experimental and simulated Au L<sub>3</sub>-edge and Rh K-edge EXAFS spectra. The best-fit bimodal models employed to simulate the EXAFS spectra are shown for each case.

and MC simulations to find stable structures. The average coordination number for the Rh<sub>38</sub> ( $N_{\text{Rh-Rh,S}}$ ) is about 6.3. The fitting results for this two-particle model are shown in Figure 12. It can be seen that the overall agreement with experiment is improved for all three samples compared to the single-particle model. The Rh K-edges match very well (Figure 12) except for the peaks at short distances which corresponding to oxidized Rh, which can not be captured by our model. The remaining differences between the simulated and experimental Au L<sub>3</sub>-edges are mainly found in the second peak, at about 2.5 Å. We do not fully understand this discrepancy. One possible reason is that there is more heterogeneity in the experimental samples than is captured in our two-particle model.

As with the single-particle model, we fit the simulated EXAFS spectra to extract the structural parameters for a quantitative comparison with the experimental values. The simulated EXAFS spectra and its fit are listed in Figure S7. The resulting structural parameters are shown in Table S6. The predicted larger Rh–Au NP in the 0.9:0.1 sample contains 20% Au, *i.e.*  $X_{\text{Au,L}} = 0.2$  and the degree of compositional segregation  $S_{\text{Au-Rh}} = 3.3$ . The fraction of atoms in the larger NP is  $X_L = 0.51$ , and the average coordination,  $N_{\text{M-M,L}} = 10.1$ . For Rh<sub>0.7</sub>Au<sub>0.3</sub>,  $X_{\text{Au,L}} = 0.4$ ,  $X_L = 0.75$ ,  $S_{\text{Au-Rh}} = 2.0$ , and  $N_{\text{M-M,L}} = 9.7$ . For Rh<sub>0.5</sub>Au<sub>0.5</sub>,  $X_{\text{Au,L}} = 0.7$ ,  $X_L = 0.72$ ,  $S_{\text{Au-Rh}} = 1.3$ , and  $N_{\text{M-M,L}} = 10.0$ . These parameters are in agreement with the prediction made by the analytic model presented above, while the atomistic simulations provide more details on the actual elemental distribution. For all samples, the segregation of Rh and Au is clear from the large Au grain sizes in the optimal structures for all samples.

In the above heterogeneous model, Rh38 was selected to represent the small Rh NPs because it gave the best overall fit simultaneously to all the samples. As a sensitivity test for the choice of Rh38, we performed the same fit using Rh201 and Rh13. The results are shown in Figure S8 and S9, respectively. It can be seen that the fit for the Au L<sub>3</sub>-edge of the Rh<sub>0.5</sub>Au<sub>0.5</sub> sample is less accurate when Rh201 is employed. When Rh13 is employed, the fits for the Rh<sub>0.9</sub>Au<sub>0.1</sub> and Rh<sub>0.7</sub>Au<sub>0.3</sub> samples degraded especially on the Rh K-edge.

### 3 Conclusions

We have employed various structural characterization techniques including S/TEM, EXAFS, and atomistic simulation to determine the atomic structures of Rh–Au NPs synthesized by microwave-assisted method. Initially, using standard experimental TEM and XRD measurements, we were misled into believing that our Rh–Au NPs were relatively uniform random-alloys. EXAFS data of these particles, combined with theoretical modeling, indicated that no single-particle model was consistent with the experimental data. With the aid of high-resolution (S)TEM, the synthesized Rh–Au NPs of different compositions are found to have a bimodal distribution, in which there exist ultrasmall pure Rh NPs and larger Rh–Au alloy NPs. An EXAFS analysis, based upon a two-particle model with sizes from (S)TEM, provide quantitative structural information including coordination numbers of pure Rh and Rh–Au NPs, compositions of Rh–Au NPs, and degrees of segregation in the Rh–Au NPs. Finally, atomistic simulations were used to fit

the experimental EXAFS spectrum. The best-fit atomic structures, again using a two-particle model, are in agreement with the results obtained by EXAFS analysis. In summary, we demonstrated that this range of structural characterization techniques combined with modeling is capable of reconstructing the atomic structures of heterogeneous NPs more accurately and completely than either technique alone.

## 4 Acknowledgments

Funding for this work was provided by the National Science Foundation under grants CHE-1534177, (G.H. and R.M.C.), CHE-1807847 (S.M.H. and G.H.), CHE-1534630 (J.C.Y.), and CHE-1534184 (AIF). We also appreciate support from the Welch Foundation (F-0032, F-1738, and F-1841). The authors acknowledge the facilities support provided at the Synchrotron Catalysis Consortium (U.S. DOE Grant No. DE-SC0012335). This research made use of resources from the Center for Functional Nanomaterials, which is a U.S. DOE Office of Science Facility, at Brookhaven National Laboratory under Contract No. DE-SC0012704. Additional exploratory microscopy was also performed at the National Center for Electron Microscopy in the Molecular Foundry, which is supported by the Office of Science, Office of Basic Energy Sciences, of the U.S. Department of Energy under Contract No. DE-AC02-05CH11231. Computational resources were provided by the National Research Scientific Computing Center and the Texas Advanced Computing Center.

## 5 Experimental and computational methods

### 5.1 Synthesis

Metal salts (0.1 mmol total) were co-dissolved in 5 mL of ethylene glycol (EG) using sonication and vortexing in a 20 mL glass scintillation vial. Separately, polyvinylpyrrolidone (PVP) (222 mg, 0.2 mmol on a monomer basis) and NaBH<sub>4</sub> (5.6 eqv. based on the HAuCl<sub>4</sub>·3H<sub>2</sub>O concentration) was weighed and transferred using 15 mL of EG to a 50 mL single neck round bottom (RB) flask. HAuCl<sub>4</sub>·3H<sub>2</sub>O (49%, Strem), RhCl<sub>3</sub>·xH<sub>2</sub>O (38-41%, Strem), PVP (<M.W.> = 58000, Alfa Aesar), EG (Certified, Fisher) were used without further purification. Thereafter a reflux condenser was connected to the RB flask and the whole apparatus was placed inside the microwave cavity. A variable power method was used to ramp the temperature inside the microwave cavity to 150 ° C with the reaction mixture stirred continuously. The pre-mixed metal salt solution (RhCl<sub>3</sub>·xH<sub>2</sub>O + HAuCl<sub>4</sub>·3H<sub>2</sub>O) in EG was then added to the PVP and maintained at 150 ° C using a dual-programmable syringe pump at a rate of 100–150 mL/h (2–3 mmol h<sup>-1</sup>). A MARS 5 microwave system (CEM Corp.) operating with a fiber-optic temperature feedback control (RTP-300+, ±0.1 ° C) and a maximum controllable power of up to 1600 W was used in all the reactions. The reaction mixture was maintained at 150 ° C for 30 minutes after which reaction was quenched using ice-water bath. The NPs were purified by selective precipitation after adding 70 mL acetone followed by vortexing and ultracentrifugation at 5500 RPM for 5 mins. A second cycle was carried out using 15 mL ethanol for dissolution and 75 mL hexanes for precipitation followed by ultracentrifugation.

gation (5500 RPM, 5 min). The resulting NPs were stored as solid-polymer film under ambient conditions using 50 mL polypropylene tubes.

## 5.2 Characterization

Powder X-ray diffraction studies were carried out using Spider diffractometer (Rigaku Corporation) operated at 40 kV and 40 mA using a Cu K $\alpha$  source ( $\lambda = 1.5418 \text{ \AA}$ ).

Transmission electron microscopy samples were prepared by dispersing NP-PVP composite in ethanol followed by sonication and vortexing in order to completely dissolve the composite. The resulting solution was drop casted onto a support of a 200-mesh copper Formvar grid (Ted Pella Inc.) and dried in air. Low-resolution transmission electron microscopy (TEM) was performed on an FEI Tecnai Transmission Electron Microscope. Size measurements and analysis of the NPs was done using ImageJ software. To obtain the mean diameter and standard deviation of NPs, a minimum of 250 manual measurements were carried out for each sample using ImageJ High resolution TEM images, high-angle annular dark field scanning transmission electron microscopy (HAADF-STEM) images, and EDS spectra were obtained using a JEOL 2010F TEM instrument equipped with an Oxford EDS detector. The operating voltage was 200 KeV and point to point resolution was 0.19 nm.

Trace metal grade hydrochloric acid (HCl, JT Baker, 36.5 – 38.0%) and nitric acid (JT Baker, 69.0 – 70.0%) were used to perform ICP analysis. For ICP-OES analysis, Rh<sub>x</sub>Au<sub>1-x</sub> alloy NPs were thermally digested using EasyPrep Plus Vessels under microwave heating. Approximately 2 mg of PVP-NP composites were added to  $\approx 10$  ml of aqua regia, prepared using trace metal acids, with precise weight determination. After attaining the desired temperature of 150 °C (1st stage ramp: temperature increase from 25 °C to 100 °C in 60 min, 2nd stage ramp: temperature increase from 100 to 150 °C in 45 min), digestion was continued at 150 °C for 3 more hrs following which the reaction mixtures were cooled down to room temperature. Solutions obtained thus were diluted using 2% trace metal grade HCl before being analyzed.

## 5.3 EXAFS measurement and data fitting

The synthesized Rh–Au NPs with nominal Rh: Au compositions: 90:10, 70:30, and 50:50 were probed with EXAFS method. Besides, a sample of pure Rh NPs was also studied. All investigated samples were ground with BN and pressed into pellets with diameter 13 mm. For all samples we carried out measurements at room temperature in air. Measurements have been carried out in transmission and fluorescence modes. We analyze the results obtained in transmission mode since the quality of obtained spectra was higher. The radiation from the storage ring was monochromatized by a Si(220) double-crystal monochromator. For Rh K-edge, monochromator was fully tuned, while for measurements at Au L<sub>3</sub>-edge 20% detuning was used. Intensity of X-rays before and after the sample was measured by two ionization chambers. For measurements at Rh K-edge  $I_0$  detector was filled with pure argon, while for measurements at Au L<sub>3</sub>-edge a mixture of 10% Ar and 90% N<sub>2</sub> was used. For  $I_1$  detector argon and krypton 1:1

mixture was used.

Here we analyze Rh K-edge and Au L<sub>3</sub>-edge EXAFS in Rh<sub>0.7</sub>Au<sub>0.3</sub> and Rh<sub>0.5</sub>Au<sub>0.5</sub> NPs. Conventional least-square fitting to theoretical standards, as implemented in FEFFIT code<sup>15</sup>, was applied, but in this case data from both absorption edges were fitted simultaneously to obtain a structure model, consistent with all available experimental information. We analyze the contributions from the first coordination shell only. For NPs, the fitted variables were coordination numbers  $N$ , average distances  $\langle R \rangle$  and MSRD factors  $\sigma^2$  for Rh–Rh, Rh–Au, Au–Au and Au–Rh pairs. We constrain  $\langle R \rangle$  and  $\sigma^2$  for Rh–Au pair to be equal to  $\langle R \rangle$  and  $\sigma^2$  for Au–Rh pair. Initially we did not apply any constraints on coordination numbers, but it resulted in very large uncertainties for structural parameters. Hence we set  $N_{\text{AuRh}} = \frac{0.72}{0.28} N_{\text{RhAu}}$  for Rh<sub>0.7</sub>Au<sub>0.3</sub> NPs and  $N_{\text{AuRh}} = \frac{0.46}{0.54} N_{\text{RhAu}}$  for Rh<sub>0.5</sub>Au<sub>0.5</sub>, where  $\frac{0.72}{0.28}$  and  $\frac{0.46}{0.54}$  terms reflect the ratio of Rh and Au atoms in the investigated NPs, calculated from the values of absorption edges as shown in Table 1. Theoretical phases and amplitudes were obtained in self-consistent *ab-initio* calculations with FEFF8.5 code<sup>16</sup> for bulk material. The complex exchange-correlation Hedin-Lundqvist potential and default values of muffin-tin radii as provided within the FEFF8.5 code were employed. For Rh K-edge data fitting was carried out in the range from  $R_{\text{min}} = 2.1 \text{ \AA}$  up to  $R_{\text{max}} = 3.4 \text{ \AA}$ . Fourier transform was carried out in the  $k$  range from 3.0–14.0  $\text{\AA}^{-1}$ . For the Au L<sub>3</sub>-edge the values  $\Delta E_0 = 0.1(4) \text{ eV}$  and  $S_0^2 = 0.89(5)$  were obtained from the fit of Au foil EXAFS data. For Au L<sub>3</sub>-edge fitting was carried out in the range from  $R_{\text{min}} = 1.7 \text{ \AA}$  up to  $R_{\text{max}} = 3.6 \text{ \AA}$ . Fourier transform was carried out in the  $k$  range from 3.0–10.0  $\text{\AA}^{-1}$ .

## 5.4 Density functional theory

The density functional theory (DFT) calculations were carried out using the Vienna *ab initio* simulation package<sup>17,18</sup>. All calculations were spin-polarized. Core electrons were described with the projector augmented-wave (PAW) method.<sup>19,20</sup> The Kohn-Sham wave functions for the valence electrons were expanded in a plane-wave basis set with an energy cutoff of 300 eV. The exchange-correlation energy was treated within the framework of the generalized gradient approximation. Specifically, PBEsol<sup>21</sup> was used, which is a modified form of Perdew-Burke-Ernzerhof (PBE) functional designed to improve lattice parameters and surface energies in solids. A single  $\Gamma$ -point was sufficient for integration of the reciprocal space due to the finite nature of the NPs. A unit cell of  $5 \times 5 \times 5$  was used to model the Au bulk and simulate the EXAFS spectrum for Au foil. A  $k$ -points mesh of  $2 \times 2 \times 2$  was used for this periodic model.

## 5.5 EXAFS simulation

We attempt to reconstruct 3D atomic structures of the synthesized Rh–Au NPs with atomistic simulations. Specifically, we propose a broad variety of atomic models for Rh–Au NPs. The goodness of fit for the proposed structures to the structures of real NPs are examined by comparing the simulated EXAFS spectra of the proposed models with experimental EXAFS spectra. Models with EXAFS spectra in close resemblance to the experimental EXAFS

spectra are considered to be good representative structures for the synthesized Rh–Au NPs.

To simulate the EXAFS spectra of atomic models, an ensemble of equilibrium structures at finite temperatures is needed. In this work, Monte Carlo (MC) simulations are employed to sample the equilibrium structures. And, we developed empirical potentials in the framework of modified embedded-atom method (MEAM)<sup>22,23</sup> to describe atomic interactions in the Rh–Au system.

In MEAM, the total energy of a metallic system is calculated as

$$E = \sum_i [F(\bar{\rho}_i) + \frac{1}{2} \sum_{j \neq i} \Phi(R_{ij})]. \quad (7)$$

In the equation, the first term is the embedding energy of atom  $i$  which is embedded into the electron density  $\bar{\rho}_i$  and the second term is the core-core pair interaction between atoms  $i$  and  $j$  separated by a distance  $R_{ij}$ . Here,  $\bar{\rho}_i$  is the background electron density at the center of atom  $i$  obtained by superposing the electronic densities from its surrounding atoms. To compute  $\bar{\rho}_i$ , we chose an FCC lattice as the reference structure of pure Rh–Rh and Au–Au potentials and Rh<sub>3</sub>Au crystal of L1<sub>2</sub> is used as the reference structure for Rh–Au cross-potentials. The detailed formula of the MEAM potentials could be found in Ref. 22, 24, 25, and 26.

The parameters for the developed Rh–Au MEAM potentials are given in Tables S1 and S2. The employed MEAM potentials for pure Rh and Au metals were similar to those published in Ref. 22, with some renormalized scaling factors in the atomic charge densities.<sup>24</sup> Besides, the parameters of pure Rh and Au metals are tuned to reproduce the experimental EXAFS spectra of Rh and Au foils. The parameters of cross-potential describing Rh–Au interactions are optimized based on our DFT results for the lattice constant, the bulk modulus, and the heat of formation of Rh<sub>3</sub>Au L1<sub>2</sub> crystal.

The MC simulation method employed in this work was implemented based on the Metropolis algorithm<sup>27</sup>, in which successive configurations were generated in proportion to the probabilities of a configuration occurring in the equilibrium ensemble. Starting from a given atomistic structure of the alloy system, we continuously tried out the configuration transformations of the system to reach the thermodynamically equilibrium ensembles. At each MC step, the energy difference  $\Delta E$  associated with a configuration change of the system was evaluated using our developed MEAM potentials. If  $\Delta E < 0$  (energy-decreasing process), the new configuration would always be retained, while if  $\Delta E > 0$  (energy-increasing process), the new configuration would be accepted with the probability  $\exp(\Delta E/k_B T)$ . Here,  $k_B$  is the Boltzmann constant and  $T$  is the temperature. We modeled the vibrational processes in the Rh–Au systems in this work through imposing displacements (in random directions) to randomly selected atoms as a type of configuration transformation in the MC simulations. For bulk systems, the volume of the simulation cell is allowed to change in response to the external pressure set to 1 bar. To simulate the EXAFS spectrum, we feed 200 snapshots of the sampled equilibrium structures by MC simulations to FEFF6-lite program<sup>15</sup>, which is an *ab-initio* software capable of calculat-

ing scattering properties of photo-excited electrons out of given atomic structures.

Using the above methods, we can well reproduce the experimental EXAFS spectra for Au and Rh foils as shown in Figure S3(a) and (b), respectively. Furthermore, the developed Rh–Au potentials can also well reproduce the simulated EXAFS spectra of Au L<sub>3</sub> and Rh K-edges of truncated-octahedral pure Au and Rh NP201 obtained with DFT as shown in Figure S3(c) and (d), respectively. We further tested the capability of the Rh–Au potentials by comparing the simulated EXAFS of Au L<sub>3</sub> and Rh K-edges of a Rh<sub>0.75</sub>Au<sub>0.25</sub> random alloyed NP201 by MEAM with the results obtained with DFT. The comparison is shown in Figure S4. For all the comparisons of EXAFS spectra, we quantify the comparison by extracting the structural parameters via fitting to the EXAFS spectra. The resulted structural parameters are shown in Tables S3 and S4. Overall, the developed MEAM potentials can well reproduce the experimental EXAFS spectra and DFT-generated EXAFS spectra. The developed Rh–Au potentials can also make reliable predictions on the thermodynamics of Rh–Au alloys. As shown in Figure S5, we calculated the formation energies of Rh–Au NP140 of different elemental distributions with both DFT and MEAM. It can be seen the results of MEAM potentials are in good agreement with DFT results.

## Notes and references

- 1 S. T. Hunt, M. Milina, A. C. Alba-Rubio, C. H. Hendon, J. A. Dumesic and Y. Román-Leshkov, *Science*, 2016, **352**, 974–978.
- 2 A. S. Lapp, Z. Duan, N. Marcella, L. Luo, A. Genc, J. Ringnalda, A. I. Frenkel, G. Henkelman and R. M. Crooks, *J. Am. Chem. Soc.*, 2018, **140**, 6249–6259.
- 3 H. Li, L. Luo, P. Kunal, C. Bonifacio, Z. Duan, J. Yang, S. Humphrey, R. Crooks and G. Henkelman, *J. Phys. Chem. C*, 2018, **122**, 2712–2716.
- 4 G. W. Piburn, H. Li, P. Kunal, G. Henkelman and S. M. Humphrey, *ChemCatChem*, 2018, **10**, 329–333.
- 5 L. Luo, Z. Duan, H. Li, J. Kim, G. Henkelman and R. Crooks, *J. Am. Chem. Soc.*, 2017, **139**, 5538–5546.
- 6 S. Seraj, P. Kunal, H. Li, G. Henkelman, S. M. Humphrey and C. Werth, *ACS Catal.*, 2017, **7**, 3268–3276.
- 7 S. García, L. Zhang, G. W. Piburn, G. Henkelman and S. M. Humphrey, *ACS Nano*, 2014, **8**, 11512–11521.
- 8 L. Piccolo, Z. Y. Li, I. Demiroglu, F. Moyon, Z. Konuspayeva, G. Berhault, P. Afanasiev, W. Lefebvre, J. Yuan and R. L. Johnston, *Sci. Reports*, 2016, **8**, 35226.
- 9 Y. Li, D. Zakharov, S. Zhao, R. Tapper, U. Jung, A. Elsen, P. Baumann, R. Nuzzo, E. Stach and A. Frenkel, *Nat. Commun.*, 2015, **6**, 7583.
- 10 A. I. Frenkel, *Chem. Soc. Rev.*, 2012, **41**, 8163–8178.
- 11 A. I. Frenkel, S. Nemzer, I. Pister, L. Soussan, T. Harris, Y. Sun and M. H. Rafailovich, *J. Chem. Phys.*, 2005, **123**, 184701.
- 12 D. F. Yancey, S. T. Chill, L. Zhang, A. I. Frenkel, G. Henkelman and R. M. Crooks, *Chem. Sci.*, 2013, **4**, 2912–2921.
- 13 Z. Duan, Y. Li, J. Timoshenko, S. T. Chill, R. M. Anderson, D. F. Yancey, A. I. Frenkel, R. M. Crooks and G. Henkelman, *Catal. Sci. Technol.*, 2016, **6**, 6879–6885.
- 14 Z. Chen, Z. Duan, Z. Wang, X. Liu, L. Gu, F. Zhang, M. Dupuis and C. Li, *ChemCatChem*, 2017, **9**, 3641–3645.
- 15 S. I. Zabinsky, J. J. Rehr, A. Ankudinov, R. C. Albers and M. J. Eller, *Phys. Rev. B*, 1995, **52**, 2995–3009.
- 16 J. J. Rehr, J. J. Kas, F. D. Vila, M. P. Prange and K. Jorissen, *Phys. Chem. Chem.*

- Phys.*, 2010, **12**, 5503–5513.
- 17 G. Kresse and J. Furthmüller, *Comput. Mater. Sci.*, 1996, **6**, 15–50.
- 18 G. Kresse and J. Furthmüller, *Phys. Rev. B*, 1996, **54**, 11169.
- 19 P. E. Blöchl, *Phys. Rev. B*, 1994, **50**, 17953.
- 20 G. Kresse and D. Joubert, *Phys. Rev. B*, 1999, **59**, 1758–1775.
- 21 J. P. Perdew, A. Ruzsinszky, G. I. Csonka, O. A. Vydrov, G. E. Scuseria, L. A. Constantin, X. Zhou and K. Burke, *Phys. Rev. Lett.*, 2008, **100**, 136406.
- 22 M. I. Baskes, *Phys. Rev. B*, 1992, **46**, 2727–2742.
- 23 M. I. Baskes and R. A. Johnson, *Model. Simul. Mater. Sci. Eng.*, 1994, **2**, 147.
- 24 G. Wang, M. A. V. Hove, P. N. Ross and M. I. Baskes, *J. Chem. Phys.*, 2004, **121**, 5410–5422.
- 25 M. I. Baskes, J. E. Angelo and C. L. Bisson, *Model. Simul. Mater. Sci. Eng.*, 1994, **2**, 505.
- 26 M. Baskes, *Mater. Chem. Phys.*, 1997, **50**, 152 – 158.
- 27 N. Metropolis, A. W. Rosenbluth, M. N. Rosenbluth, A. H. Teller and E. Teller, *J. Chem. Phys.*, 1953, **21**, 1087–1092.